Combined Infrared-Ultrasonic Positioning System to improve the Data Availability

Elena Aparicio-Esteve, Jesús Ureña, *Senior Member, IEEE*,
Álvaro Hernández, *Senior Member, IEEE*, José M. Villadangos

***Abstract*— Many indoor positioning applications related to accurate monitoring and tracking targets require centimeter precision. Infrared- and ultrasound-based systems represent a feasible approach providing high robustness against interference. Furthermore, their combination may achieve better performance by mitigating their complementary drawbacks, covering larger areas and improving the availability of positioning measurements. In this context, this work presents the proposal and experimental evaluation of a tightly-coupled fusion method that uses an Extended Kalman Filter to merge an infrared- and a ultrasound-based positioning system. An outlier detection method is considered to select measurements with an adequate performance. Experimental results reveal that the infrared and ultrasound systems are unable to position in 4.08% and 26.06% of locations, whereas the combined infrared-ultrasound system has 100% of availability. In addition, the merged solution achieves less than 4 cm of positioning error in 90% of cases, outperforming the IR and US systems when they work independently.**

***Index Terms*— Extended Kalman Filter, Infrared, Local Positioning System (LPS), Tightly-coupled fusion, Ultrasound**

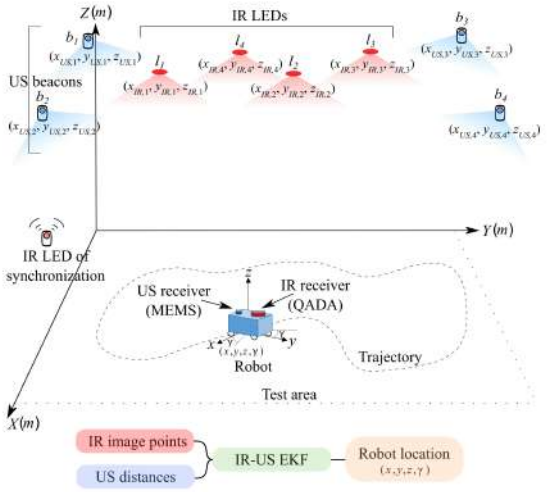

I. Introduction

The emergence and spreading of multiple Location-based Services (LBS) and applications in recent years have boosted the proposal and development of different positioning systems. The last goal for these systems is to obtain the position of a certain target, which might be a person, a mobile robot or drone, or even a passive object of interest. Whereas the main challenges about positioning outdoors have already been solved by GNSS (Global Navigation Satellite Systems), the context is completely different indoors, where diverse technologies are often involved in the development of the so-called Local Positioning Systems (LPS). The choice of a certain sensory technology sometimes depends on the requirements defined by the final application [1], where aspects such as accuracy, availability, range, or even cost, are commonly considered.

This work has been possible thanks to the Ministry of Science, Innovation and Universities (project INDRI, ref. PID2021-122642OB-C41, project ALONE, ref. TED2021-131773B-I00, and project PoM, ref. PID2019-105470RA-C33), to the Community of Madrid (project QADIR, ref. CM/JIN/2021-027, and project RACC, ref. CM/JIN/2021-016) and the European Science Foundation under Grant CA19111-NEWFOCUS

Elena Aparicio-Esteve is with the Department of Signal Processing and Communications, Universidad Rey Juan Carlos, Fuenlabrada, Spain. Jesús Ureña, Álvaro Hernández and José M. Villadangos are with the Electronics Department, University of Alcalá, Alcalá de Henares, Spain (e-mail: elena.aparicio@urjc.es; jesus.urena@uah.es; alvaro.hernandez@uah.es; jm.villadangos@uah.es).

Generally speaking, nowadays, it is possible to find positioning solutions based on optical sensors, radio frequency (RF), acoustic sensors, or even magnetic sensors, among others. None of them is definitive and many times the optimal approach for some applications comes up as a combination of several technologies. Furthermore, the massive use of intelligent devices worldwide, such as tablets or smartphones, has influenced the appearance of new proposals based on the possibilities offered by them. These proposals are mainly based on the use of their communications links and sensors, where it is worth mentioning networks such as WiFi, Bluetooth Low Energy (BLE) [2]–[4], or ultra-wide band (UWB) [5]. This one has recently become relevant, since it is capable of achieving positioning errors quite below the performance shown by other RF technologies (lower than decimetres) [6].

As for the infrared-based LPSs (IRLPS), they are becoming more and more interesting since the LED lamps are already available in most indoor spaces [7]–[9]. From a computational point of view, they present the drawback related to the velocity of light, the reason why they often apply different positioning algorithms from those based on times-of-arrival (ToA), while also reducing effects coming from multiple reflections and multipath [10]. A key aspect for IRLPS is the receiver. Some approaches are based on imaging sensors, which involve demanding computer vision methods in the implementation [11]. On the other hand, another approach is the use of pho-

todetectors, either alone [12] [13] or forming arrays [14]–[16]. A typical case is Quadrant Photodiodes (QP) together with an aperture [17], as well as other examples, such as Position-Sensitive Detectors (PSD) [18] or prism-based designs [19]. Common positioning methods for these systems are often based on fingerprinting from Received Signal Strenght (RSS) [20] [21], and triangulation or multilateration by measuring the Angles-of-Arrival (AoA).

Concerning ultrasound-based LPSs (ULPS) [22]–[26], they typically consist in the deployment of some, transmitting or receiving, beacons at known positions in the environment under analysis, where it is possible to estimate a target's position [27], [28]. In this case, most proposals are based on determining the corresponding ToAs, or the Time-Differences-of-Arrival (TDoA), between the beacons and the target, which are used afterwards to apply a spherical or hyperbolic trilateration, respectively [29]. These systems are able to achieve errors in the range of decimeters, while keeping a relatively low cost.

High-level fusion filtering can be applied as well. For that purpose, the Kalman Filter (KF) and its different variations are suitable to improve the final accuracy and coverage when dealing with the fusion of several positioning technologies. KF methods are capable of estimating the target's position by merging different sources of information, such as the previous estimated positions and the current measurements, achieving better results when compared with other straightforward positioning algorithms. It is also common to deal with non-linear systems, which require the use of appropriate versions of the filters: Extended Kalman Filter (EKF) or Unscented Kalman Filter (UKF), for instance. In the case of ULPS, the work in [30] compares the performance of EKF, UKF and H_∞ filters, showing similar accuracies and showing that the main differences lie on the implementation issues. Another example can be found in [31] that uses an EKF for a single IRLPS to obtain a positioning error below $10\,$cm. In [32], an ULPS and an Inertial Measurement Unit (IMU) are combined using an EKF to obtain a positioning error average of $3.7\,$cm, whereas in [33] an UKF is used to obtain an opto-acoustic and inertial indoor localization system, providing an average error of $3.2\,$cm.

For integration proposes, there are two common strategies: the loosely-coupled and the tightly-coupled integration. As stated in [34], the basic difference between them is the type of data shared from the different positioning systems to obtain an unique position estimation. In the case of using a loosely-coupled filter, every independent positioning system needs to process its raw data to obtain a particular position, so the positions estimated by each system are the inputs of the integration filter. In the case of a tightly-coupled filter, the raw measurements from every independent positioning system are directly the inputs of the integration filter. The main advantage of the tight integration is the possibility of updating the final position also in scenarios with poor signal quality or limited coverage for the particular systems.

In this context, our previous work [35] dealt with the experimental evaluation of a loosely-coupled fusion KF to merge the positions independently obtained by two positioning systems, one IR-based and another US-based. This method required that both systems completed their own positioning algorithms independently before applying any fusion. If one of them does not have enough valid measurements, the fusion cannot be applied. In particular, in [35] the achieved absolute errors in the XY plane for the position estimation was below $7\,$cm in 90% of cases, and no estimation of coordinate z was done. The current work presents a tightly-coupled EKF method to combine an IRLPS and an ULPS. Both systems are assumed to cover a common area, in which the corresponding measurements are acquired simultaneously. This fusion method allows the reliability and availability to be significantly increased in the coverage area. The EKF provides a way to consider previous estimates, motion models and fresh measurements, even when some of these measurements are missing or they are discarded because they present a reduced accuracy, i.e., they are detected as outliers. The final results imply a more robust estimation of the target's position. The proposal has been successfully validated, not only by simulation, but also by experimental tests, which have been carried out in a real scenario of approximately 4×4 m^2. The main contributions of this work are:

- The fusion of two LPSs based on different technologies, infrared and ultrasound, in order to mitigate the particular drawbacks from each one, and complement and enhance their final performance, in terms of accuracy and availability.
- The adaptation of a merging method, based on an EKF, to combine very different raw measurements (in this case distances from the ULPS and image points from the IRLPS), in order to obtain a more robust estimation of the final position.
- The fully validation of the proposal, by simulation and experimental tests, in a real scenario, where numerous trials have been carried out at different positions and following some trajectories of interest. Positioning errors are below $4\,$cm for coordinates x and y in 90% of cases, also increasing the availability of the global system when compared with independent LPSs.

The rest of the manuscript is organised as follows: Section II describes the infrared and ultrasonic LPSs, detailing their distribution and features; Section III presents the EKF, particularized hereinafter for the fusion of both LPSs' raw measurements, including also the outliers' detection and considering the different position of the IR and US receivers; Section IV provides the simulation results, whereas Section V deals with some experimental tests and real characterization of the whole system; and, finally, conclusions are discussed in Section VI.

II. Description of the IR-US Proposed System

The proposed infrared-ultrasound positioning unit cell (IR-US) is based on: 1) a set of IR LED emitters l_i and US beacons b_j located at known positions in the ceiling; 2) an US and an IR receiver placed on top of a mobile robot; and 3) a synchronism module. Fig. 1 presents a general scheme of the proposal. It is assumed hereinafter that the mobile robot can move in a certain plane (for example, on the floor). The pose

of the mobile robot is then denoted as (x, y, z, γ), where γ is the rotation angle around the Z axis of the receiver.

The positioning system's behavior on a single cell is analysed in this work. It should be noted that this proposal, focused on a cell, is easy to scale whether positioning in a larger scenario is necessary by simply adding more cells to the new scenario. This principle of operation based on unit cells has already been implemented in previous works [36], [37], with positioning cells ranging from 2 m to 10 m. In this way, the proposal described hereinafter can be considered as a 3D IR-US positioning cell to obtain the position and orientation of a mobile robot moving on a horizontal floor inside a dimension of 2×2 m^2.

The synchronism module consists of an IR emitter driven by a microcontroller, that emits a pulse at 5 Hz. This synchronism pulse is detected by photodetectors located at each IR and US beacon of the positioning systems, as well as in the receivers. When the receivers detect the pulse, they begin to acquire at the same time that the emitters' transmissions start, so that both positioning systems (IR and US) emit and receive simultaneously. In the following, a more in-depth analysis of both IR and US systems is presented.

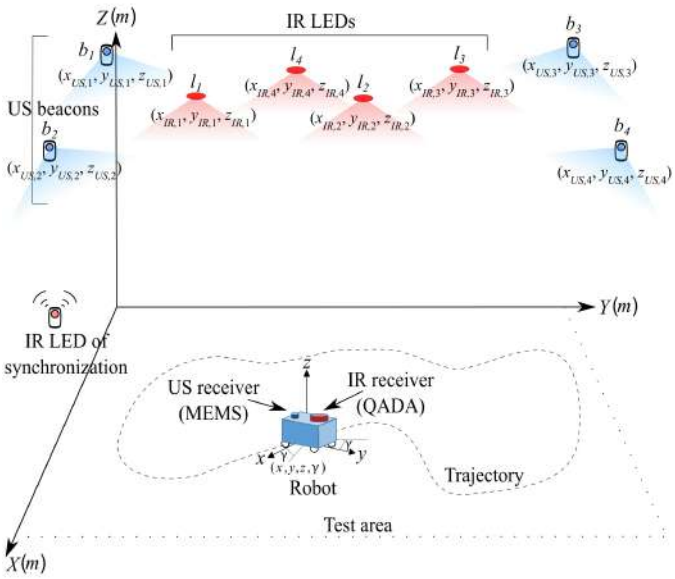

Fig. 1: Global overview of the proposed IR-US LPS.

A. Description of the Infrared Local Positioning System

The proposed infrared local positioning system (IRLPS) is based on a set of four emitters LED l_i, $i = \{1, 2, 3, 4\}$, and a receiver. Every LED l_i transmits a BPSK (Binary Phase Shift Keying) 1151-bit LS sequence c_i modulated with a carrier of 25 kHz and a modulation symbol of one carrier period [38]. The reception system consists of a Quadrant photodiode Angular Diversity Aperture (QADA), which is a circular photoreceptor QP50-6-18u-TO8 [39] with a square aperture placed on top of it at a height h_{ap}, a synchronism detector, a filtering stage and an acquisition system STM32F469I Discovery [40]. The sampling frequency is set at 250 kHz. The incoming acquired signals are stored in a micro-SD at the receiver for further processing in a computer.

The principle of operation in the proposed IRLPS is that the light emitted by the LEDs passes through the centre of the aperture and illuminates the QADA receiver. Each quadrant generates a current proportional to the illuminated area on the photodiode. These four currents are transformed into voltages by means of four transimpedance amplifiers and, then, combined to provide three output signals: the sum of all quadrant voltages (v_{sum}), and the differences of voltages in the axes X (v_{lr}) and Y (v_{bt}). These three signals are acquired and processed to obtain the projections of the transmitters on the QADA's surface, which are known as the image points (x_r, y_r). This procedure is based on the correlation of the received signals v_{sum}, v_{lr} and v_{bt} with the transmitted codes c_i. The resulting correlation peaks, that represent the energy received at the QADA, are used to obtain the ratios between the difference signals and the sum signal (p_x, p_y). Afterwards, the position of the image point is estimated for each transmitter (1). Note that the intrinsic parameters have also been considered in the estimation of the image points (x_r, y_r) [41], which are: the aperture length l, the central point (x_c, y_c), the misalignment of the aperture δ, and the ratio between the expected focal length h_{ap} and the actual focal length h'_{ap}: $\lambda = h'_{ap}/h_{ap}$. The image points (x_r, y_r) of each emitter l_i are used as the input of the EKF that is explained in Section III.

$$\begin{bmatrix} x_r \\ y_r \end{bmatrix} = \frac{-l}{2} \cdot \lambda \cdot \begin{bmatrix} p_x + \delta \cdot p_y \\ -\delta \cdot p_x + p_y \end{bmatrix} + \begin{bmatrix} x_c \\ y_c \end{bmatrix} \tag{1}$$

After estimating the image point positions (x_r, y_r) for each emitter l_i, the rotation γ of the receiver around the Z axis is obtained by means of trigonometric equations [42]. Since the transmitters are arranged in a rectangle, the image points also maintain that shape. Thus, rotating the receiver at a certain angle γ around the Z axis results in a rotation γ of the image points. After the estimation of γ, the image points are rotated $-\gamma$ to align the image points and the receiver with the reference frame. This is a necessary step since the final positioning algorithm requires that the receiver has no rotation ($\gamma = 0$). Finally, the coordinates of the receiver (x, y, z) are estimated using an LSE (Least Squares Estimator) and different trigonometric considerations [38].

The behaviour of the proposed IRLPS in the test area is analysed through the Horizontal Dilution of Precision (HDOP), the Vertical Dilution of Precision (VDOP) and the Position Dilution of Precision (PDOP) (2) with simulations in a test area of 4×4 m^2, with a step resolution of 10 cm and with a distance/height between transmitters and receiver of 3.4 m. The variance of coordinates x, y, and z is denoted as σ_x^2, σ_y^2 and σ_z^2, respectively, and σ_0 is the standard deviation of the additive noise included in simulations (media $\overline{x} = 0$ and standard deviation $\sigma_0 = 10^{-4}$ V, which represents the error expected in the voltages obtained after the amplifiers of the QADA). At each point in the grid the triangulation positioning algorithm previously explained is run 50 times.

$$HDOP = \frac{\sqrt{\sigma_x^2 + \sigma_y^2}}{\sigma_0} \qquad (2)$$
$$VDOP = \frac{\sqrt{\sigma_z^2}}{\sigma_0}$$
$$PDOP = \frac{\sqrt{\sigma_x^2 + \sigma_y^2 + \sigma_z^2}}{\sigma_0}$$

Fig. 2 presents the HDOP, VDOP and PDOP when the receiver is placed on the floor (at a height of $z = 0$ m). The coordinates of each IR LED considered in the simulations are: (x_{IR}, y_{IR}, z_{IR}) = {(−1 m, 1 m, 3.4 m), (1 m, 1 m, 3.4 m), (1 m, −1 m, 3.4 m), (−1 m, −1 m, 3.4 m)}. A Gaussian noise has been introduced in the QADA output signals with a SNR = 10 dB. The transmitters' projections are also represented with black crosses in the XY plane. An increase of the HDOP at the coverage area corners with respect to the centre of the room can be clearly observed, as well as an increase of the VDOP and PDOP whether the receiver is located near the transmitters' projections.

B. Description of the Ultrasounic Local Positioning System

The ultrasonic local positioning system (ULPS) consists of a set of four emitting ultrasonic beacons b_j, $j = \{1, 2, 3, 4\}$, and a receiver. Each beacon transmits a BPSK-modulated 255-bit Kasami code with a carrier of 41.667 kHz [28] and a modulation symbol of two carrier periods. The ultrasonic receiver consists of a MEMS microphone SPU0414HR5H-SB [43], connected to an analog input of the STM32F103 microcontroller to acquire the incoming signal at $f_s = 100$ kHz with 8 bits. The detected signals are stored at the receiver in a micro-SD for further processing in a computer.

The times-of-flight (ToFs) measured allow the distances d_j between the beacons and the receiver to be estimated. These distances are obtained from the matched filtering between the received signal and the emitted Kasami codes. A non-linear equations system results from the measured distances and, in order to estimate the receiver's position (x, y, z), it is solved using an iterative approach such as the Gauss-Newton algorithm. These distances are then used as the input of the EKF that is detailed in Section III. In spherical trilateration, only three correct measurements are required to estimate the receiver's position when the beacons are placed on the ceiling. It should be noted that the algorithm dynamically adapts and solves the oversized system whether more measurements are available. More details can be found in [28], where a large coverage ULPS is described, as well as in [6], where an IRLPS is added to the ULPS and a comparison with an UWB solution is also provided.

Similarly to the analysis performed for the IRLPS, the HDOP, VDOP and PDOP of the proposed ULPS have been obtained in simulations (2) in the same test area of 4×4 m^2, with a height between transmitters and receiver of 3.4 m. The coordinates for each US beacon considered in simulations are: (x_{US}, y_{US}, z_{US}) = {(3.9 m, 3.5 m, 3.4 m), (3.9 m, −3.5 m, 3.4 m), (−3.9 m, −3.5 m, 3.4 m), (−3.9 m, 3.5 m, 3.4 m)}. The obtained results are presented in Fig. 3, when the receiver is located on the floor (at $z = 0$ m). Lower values of PDOP are observed in the ULPS with respect to the IRLPS system, but it is important to note that in the ULPS $\sigma_0 = 0.01m$ represents the error in the measurement of distances between emitters and receiver. It is worth noticing that the ULPS and IRLS have different zones with good and bad performances, what also justifies the fusion of both systems. Finally, note that the US beacon projections in the XY plane are not plotted since they are located at the room's corners, outside of the central coverage area shown in Fig. 1.

III. Particularization of the Extended Kalman Filter (EKF)

With regard to the fusion filters, it is necessary to firstly consider whether the equations involved are linear or non-linear. In addition, we can also differentiate between loosely and tightly coupled systems. In this proposal, we implement a tightly coupled algorithm in a non-linear system that uses the image points $(x_r, y_r)_i$ from the IR system and the distances d_j between the transmitters and the receiver from the US system, in order to estimate the final coordinates of the receiver (x, y, z) and the rotation γ in the Z axis, using an EKF.

The EKF is suitable for non-linear systems, relying on the covariance matrices of the state and measurement noises of the process. The EKF linearises the propagation of the estimation error covariance matrix by using the Jacobian operator in both the prediction and correction stages. The equations of the non-linear model, in state space, are given in (3), where $\mathbf{X}_k = (x, y, z, \gamma)_k$ is the estimated position and the rotation for the receiver in the Z axis, in the current state k; $\mathbf{Z}_k$ is the set of acquired measurements given by the image points $(x_r, y_r)_i$ (1) and the distances d_j; and w_k and v_k are the process and measurement noises, respectively.

$$\begin{aligned} \mathbf{X}_k &= f(\mathbf{X}_{k-1}) + w_k \\ \mathbf{Z}_k &= h(\mathbf{X}_k) + v_k \end{aligned} \qquad (3)$$

After initialising the position vector $\mathbf{X}_0$ and the estimation error covariance matrix $\mathbf{P}_0$, the recursive loop between predictions and updates starts until the system converges to the estimated final position. The prediction stage (4) estimates the a priori state vector $\hat{\mathbf{X}}_k^-$, and its covariance $\mathbf{P}_k^-$; and the update stage (5) obtains the state vector $\hat{\mathbf{X}}_k$, its covariance $\mathbf{P}_k$ and the Kalman gain $\mathbf{K}_k$. The implemented EKF uses the updated state vector from the previous iteration as initial state vector at each iteration so that $f(\mathbf{X}_{k-1}) = \mathbf{X}_{k-1}$.

$$\begin{aligned} \hat{\mathbf{X}}_k^- &= f(\hat{\mathbf{X}}_{k-1}) \\ \mathbf{P}_k^- &= \mathbf{A}_k \cdot \mathbf{P}_{k-1} \cdot \mathbf{A}_k^T + \mathbf{Q}_k \end{aligned} \qquad (4)$$

$$\begin{aligned} \mathbf{K}_k &= \mathbf{P}_k^- \cdot \mathbf{H}_k^T \cdot (\mathbf{H}_k \cdot \mathbf{P}_k{}^- \cdot \mathbf{H}_k^T + \mathbf{R}_k)^{-1} \\ \hat{\mathbf{X}}_k &= \hat{\mathbf{X}}_k^- + \mathbf{K}_k \cdot (\mathbf{Z}_k - h(\hat{\mathbf{X}}_k^-)) \\ \mathbf{P}_k &= (\mathbf{I} - \mathbf{K}_k \cdot \mathbf{H}_k) \cdot \mathbf{P}_k^- \end{aligned} \qquad (5)$$

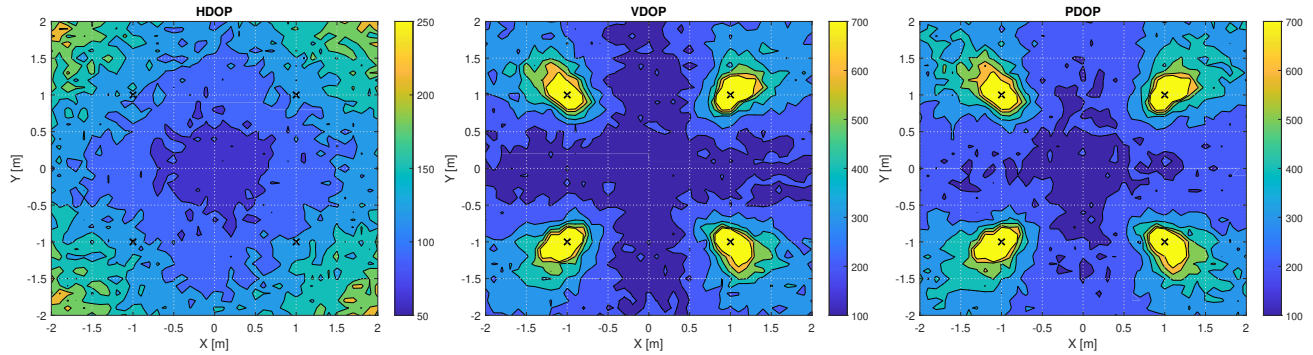

(a) (b) (c)

Fig. 2: a) HDOP; b) VDOP; c) PDOP for the proposed IRLPS in the coverage area when the receiver is placed at $z = 0\,\text{m}$ (on the floor).

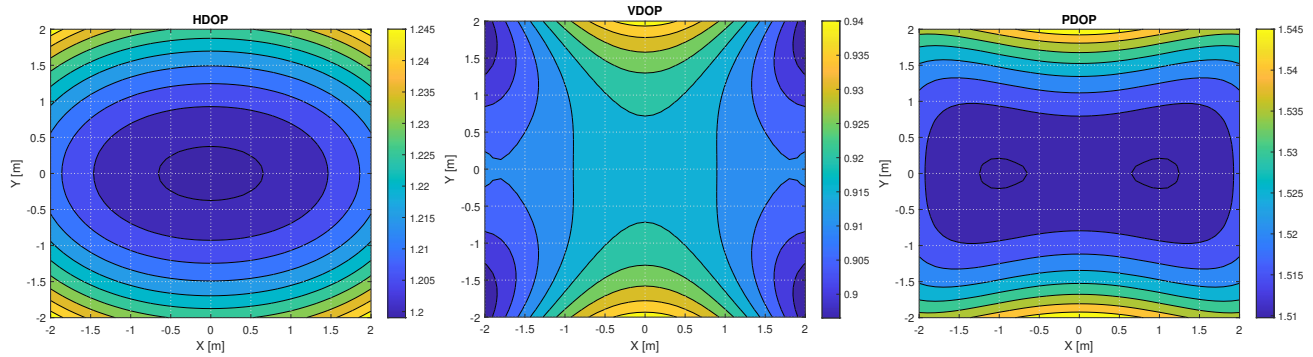

(a) (b) (c)

Fig. 3: a) HDOP; b) VDOP; c) PDOP for the proposed ULPS in the coverage area when the receiver is placed at $z = 0\,\text{m}$ (on the floor).

Where $\mathbf{Q}_k$ and $\mathbf{R}_k$ are the process and measurement noise error covariance matrices, respectively; $\mathbf{A}_k$ is the Jacobian of $f(\hat{\mathbf{X}}_{k-1})$ with respect to the state vector $\hat{\mathbf{X}}_k^-$, $\mathbf{A}_k = \frac{\partial f(\hat{\mathbf{X}}_{k-1})}{\partial \hat{\mathbf{X}}_k^-}\Big|_{\hat{\mathbf{X}}_k^-}$; and $\mathbf{H}_k$ represents the Jacobian of $h(\hat{\mathbf{X}}_k^-)$ with respect to the state vector $\hat{\mathbf{X}}_k^-$, $\mathbf{H}_k = \frac{\partial h(\hat{\mathbf{X}}_k^-)}{\partial \hat{\mathbf{X}}_k^-}\Big|_{\hat{\mathbf{X}}_k^-}$.

The covariance matrices $\mathbf{Q}_k$ and $\mathbf{R}_k$ are obtained experimentally as defined in (6) and (7-9), where σ_x^2, σ_y^2, σ_z^2 and σ_γ^2 are the variances of the measured positions (x, y, z, γ); $\sigma_{x_r}^2$, $\sigma_{y_r}^2$ and $\sigma_{x_r y_r}$ are the covariances of the image points $(x_r, y_r)_i$, and σ_d^2 is the covariance of the distances d_j that are included in the measurement set $\mathbf{Z}_k$; and i is the index of IR LEDs in our system, with $i = \{1, 2, ..., I\}$, where I is the total number of IR LEDs, and j is the index of US beacons in our system, with $j = \{1, 2, ..., J\}$, where J is the total number of US beacons.

$$\mathbf{Q}_k = \begin{pmatrix} \sigma_x^2 & 0 & 0 & 0 \\ 0 & \sigma_y^2 & 0 & 0 \\ 0 & 0 & \sigma_z^2 & 0 \\ 0 & 0 & 0 & \sigma_\gamma^2 \end{pmatrix}_k \tag{6}$$

$$\mathbf{R}_{IR,k} = \begin{pmatrix} \begin{pmatrix} \sigma_{x_r}^2 & \sigma_{x_r y_r} \\ \sigma_{x_r y_r} & \sigma_{y_r}^2 \end{pmatrix}_1 & \cdots & 0 \\ \vdots & \ddots & \vdots \\ 0 & \cdots & \begin{pmatrix} \sigma_{x_r}^2 & \sigma_{x_r y_r} \\ \sigma_{x_r y_r} & \sigma_{y_r}^2 \end{pmatrix}_I \end{pmatrix}_k \tag{7}$$

$$\mathbf{R}_{US,k} = \begin{pmatrix} \sigma_{d,1}^2 & \cdots & 0 \\ \vdots & \ddots & \vdots \\ 0 & \cdots & \sigma_{d,J}^2 \end{pmatrix}_k \tag{8}$$

$$\mathbf{R}_k = \begin{pmatrix} \mathbf{R}_{IR} & 0 \\ 0 & \mathbf{R}_{US} \end{pmatrix}_k \tag{9}$$

We calculate $h(\hat{\mathbf{X}}_k^-)$ (10) from (1) and from the estimation of the distances d_j in the US system. Note that these equations are repeated for each pair i of IR LED and image point. as well as for each US beacon-receiver pair j.

$$h(\hat{\mathbf{X}}_k^-) = \begin{bmatrix} \begin{bmatrix} x_r \\ y_r \end{bmatrix}_1 \\ \vdots \\ \begin{bmatrix} x_r \\ y_r \end{bmatrix}_I \\ d_1 \\ \vdots \\ d_J \end{bmatrix}_k = \begin{bmatrix} \frac{h_{ap}}{z+z_{t,1}} \cdot \begin{bmatrix} x + x_{IR,1} \cdot cos(\gamma) + y_{IR,1} \cdot sin(\gamma) \\ y + y_{IR,1} \cdot cos(\gamma) - x_{IR,1} \cdot sin(\gamma) \end{bmatrix} \\ \vdots \\ \frac{h_{ap}}{z+z_{t,I}} \cdot \begin{bmatrix} x + x_{IR,I} \cdot cos(\gamma) + y_{IR,I} \cdot sin(\gamma) \\ y + y_{IR,I} \cdot cos(\gamma) - x_{IR,I} \cdot sin(\gamma) \end{bmatrix} \\ \sqrt{(x - x_{US,1})^2 + (y - y_{US,1})^2 + (z - z_{US,1})^2} \\ \vdots \\ \sqrt{(x - x_{US,J})^2 + (y - y_{US,J})^2 + (z - z_{US,J})^2} \end{bmatrix}_k \tag{10}$$

A. Detection of Outliers in the EKF

In order to increase the robustness of the filter, it is important to detect if the acquired measurements from the IR and US systems (image points and distances, respectively) are outliers before including the data in the update stage of the filter.

A measurement is considered an outlier whether the difference between the actual measurement and the previous one is higher than a certain threshold. Hereinafter, we have considered a threshold of 25 cm for the distances d_k measured by the US system and 0.2 mm for the image points $(x_r, y_r)_k$ from the IR system. In the case of detecting an outlier, that measurement is discarded, and it does not enter into the combined IR-US EKF. This method assures that the criteria for discarding an outlier is similar for both systems. Note that the matrix $\mathbf{Z}_k$ only contains measures that are not considered outliers, and the dimensions of matrices $\mathbf{R}$ and $h(\hat{\mathbf{X}}_k^-)$ are updated according to $\mathbf{Z}_k$.

A summary of the implementation defined for the EKF is presented in the flowchart in Fig. 4. After the initialization, the EKF starts with the prediction step, where $\hat{\mathbf{X}}_k^-$ and $\mathbf{P}_k^-$ are estimated. The algorithm then proceeds to the update step, where it firstly determines whether the input measures are outliers and, then, sets the dimensions and values of $\mathbf{Z}_k$, $\mathbf{R}_k$ and $h(\hat{\mathbf{X}}_k^-)$ accordingly, before estimating the receiver's position given by the position vector $\mathbf{X}_k$.

B. Unifying the Reference Systems of IR and US Receivers.

Both receivers cannot be placed in the same location during the experimental tests. In reality, as depicted in Fig. 1, there is a gap between the US and IR receivers that may have an impact on the estimation of the receiver's position. Thus, we will estimate the position of the IR receiver as if it were the position of the mobile robot in order to correct the misalignment between the two receivers.

In this way, it is necessary to modify the US system equations previously used in (10). In particular, the distance d between the US transmitter and US receiver is replaced by the distance d' between the US transmitter and IR receiver. The distance l between the IR and US receivers is a known value. A summary of the problem is presented in Fig. 5.

To calculate the desired distance d', we first estimate the rotation angle θ of the robot on two consecutive locations (11).

$$\theta = \tan^{-1}\left(\frac{y_k - x_{k-1}}{x_k - x_{k-1}}\right) \tag{11}$$

After the estimation of the rotation θ, we continue with the estimation of θ' (12), which is the angle between the 2D coordinates of the US transmitter $(x_{US}, y_{US})_j$ and US receiver.

$$\tan(\theta + \theta') = \frac{y_{US,j}}{x_{US,j}} = \frac{\tan(\theta) + \tan(\theta')}{1 - \tan(\theta) \cdot \tan(\theta')}$$

$$\theta' = \tan^{-1}\left(\frac{y_{US,j} - x_{US,j} \cdot \tan(\theta)}{x_{US,j} + y_{US,j} \cdot \tan(\theta)}\right) \tag{12}$$

The third step is the estimation of the distance between the US transmitter and the IR receiver (13). To do so, we use trigonometric relations to obtain h (14) and θ'' (15).

$$d = \frac{h}{\sin(\theta'')} \tag{13}$$

$$h = d' \cdot \sin(\theta') \tag{14}$$

$$\theta'' = \tan^{-1}\left(\frac{h}{l + l'}\right) \tag{15}$$

where l' is defined as $l' = d \cdot \cos(\theta')$.

Finally, the estimation of the distance d' between the US transmitter and the IR receiver is obtained as (16).

$$d' = \sqrt{z_{US}^2 + d^2} \tag{16}$$

IV. Simulated Results

The simulated test have been carried out in a scenario of 4×4 m^2 with the IR-US transmitters located at the same positions as in Section II. In the following tests, we have adjusted the transmitters' coordinates to match the real positions of the transmitters in the experimental setup of Section V. In particular, the IR transmitters have been placed in the ceiling of the room, in its central area. The coordinates for each IR LED $i = \{1, 2, 3, 4\}$ considered in the simulations are: (x_{IR}, y_{IR}, z_{IR}) = {(3.5 m, 3.9 m, 3.4 m), (4.5 m, 3.9 m, 3.4 m), (4.5 m, 2.9 m, 3.4 m), (3.5 m, 2.9 m, 3.4 m)}. The US transmitters have been located at the corners of the room ceiling. The coordinates for each US beacon $j = \{1, 2, 3, 4\}$ considered in the simulations are: (x_{US}, y_{US}, z_{US}) = {(1 m, 6.4 m, 3.4 m), (7 m, 6.4 m, 3.4 m), (7 m, 0.4 m, 3.4 m), (1 m, 0.4 m, 3.4 m)}. On the other hand, the IR-US receivers are placed on the room floor. A Gaussian noise with a Signal-to-Noise Ratio (SNR) of 10 dB is introduced at the QADA receiver outputs and a Gaussian noise with mean 1 cm is added at the distance measurements from the ultrasonic signals.

Two trajectories are analyzed: the first one is inside an area of 2×2 m^2 (inner trajectory), whereas the second trajectory is a square with a side of 3 m (outer trajectory). The proposed trajectories are analysed using an EKF, where the measurement noise matrix $\mathbf{R}$ is diagonal with values $\sigma_{x_r}^2 = \sigma_{y_r}^2 = 10^{-7}$ mm^2, $\sigma_{x_r y_r} = 0$ mm^2 and $\sigma_d^2 = 10^{-7}$ m^2, the process noise covariance matrix $\mathbf{Q}$ has static

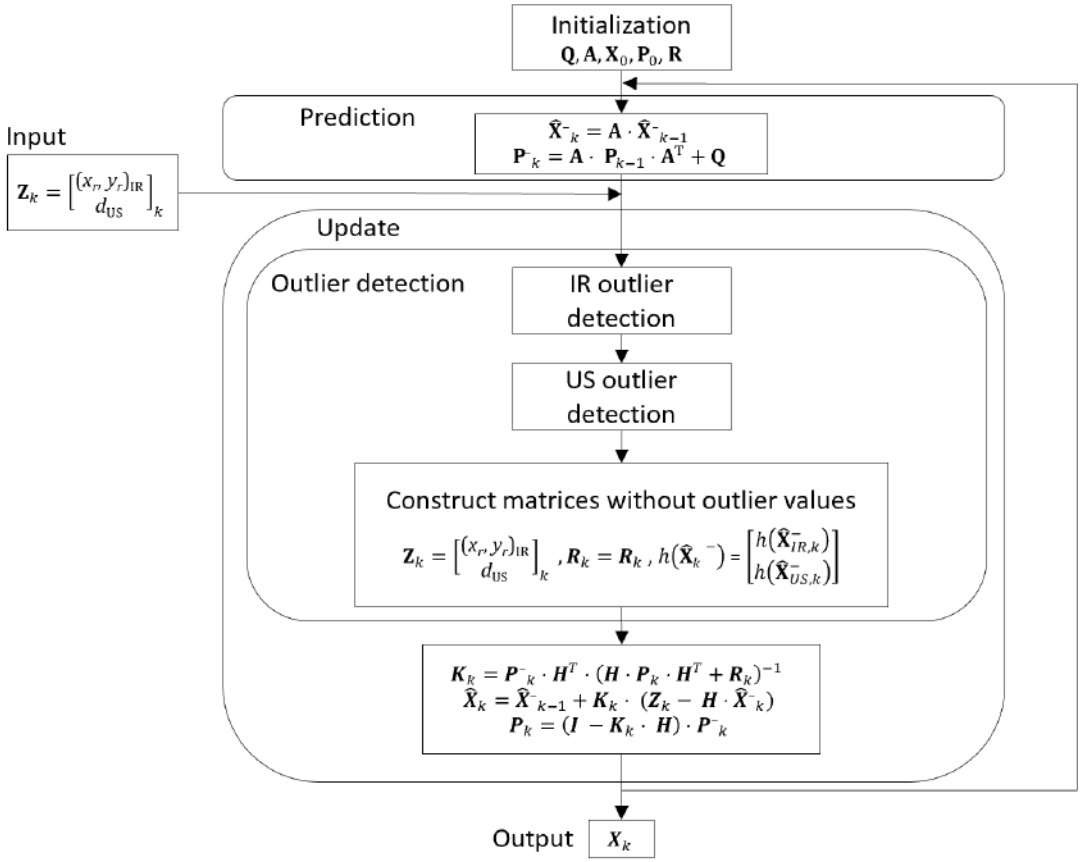

Fig. 4: Flowchart of the EKF proposed for merging the acquired US and IR measurements.

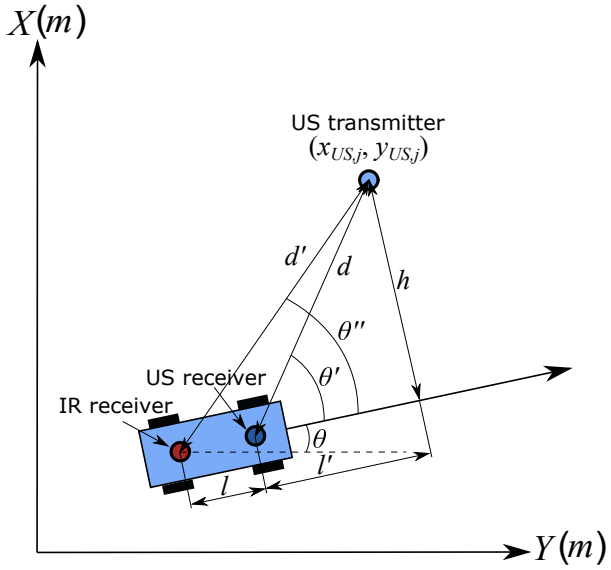

Fig. 5: 2D geometrical relations between the IR and US receivers with the US transmitter.

values $\sigma_x^2 = \sigma_y^2 = \sigma_z^2 = \sigma_\gamma^2 = 10^{-6}$ m^2, and the initial transition matrix $\mathbf{P}_0$ is diagonal with all values $\sigma^2 = 10^{-2}$. To find the noise matrix $\mathbf{R}_{IR}$, simulations were conducted in [44] using different distances between the emitters and the receiver, as well as different rotations of the receiver. The obtained results were in the order of $\sigma^2_{x_r} = \sigma^2_{y_r} = 10^{-7}$ mm^2 and $\sigma_{x_r y_r}$ achieved values between $\sigma_{x_r y_r} = -2 \cdot 10^{-7}$ mm^2 and $\sigma_{x_r y_r} = 2 \cdot 10^{-7}$ mm^2. In this work, we have chosen the average of these values. Matrices $\mathbf{P}_0$ and $\mathbf{Q}$ have been adjusted experimentally.

Fig. 6 shows the EKF estimated positions in the XY plane for both trajectories using either the IR or US system (red or blue dots, respectively), or both of them (green dots). The projections of the IR beacons are represented with a black cross, and the ground-truth of both trajectories is plotted with a black line. Note that the US beacon projections are not plotted in the XY plane since they are located at the room's corners, far away from the central coverage area shown in Fig. 1. In this simulation, 11 % of IR and US measurements are forced to be outliers (a maximum 22 % of outliers). The outliers for the US and the IR measurements are defined as random measurements in the distances and image points, with mean 10 cm and 10 μm, respectively. In addition, since the outliers are randomly located during the trajectories, both IR and US measurements can become outliers at the same time. As no movement model is implemented, the bad measurements make the independent positioning systems have large errors, which are reduced when both systems are merged.

Fig. 7 presents the CDF of the absolute positioning errors for coordinates x, y, z. obtained after repeating the complete trajectories 50 times. It can be observed how the use of a IR-US tightly coupled EKF outperforms the use of only one of

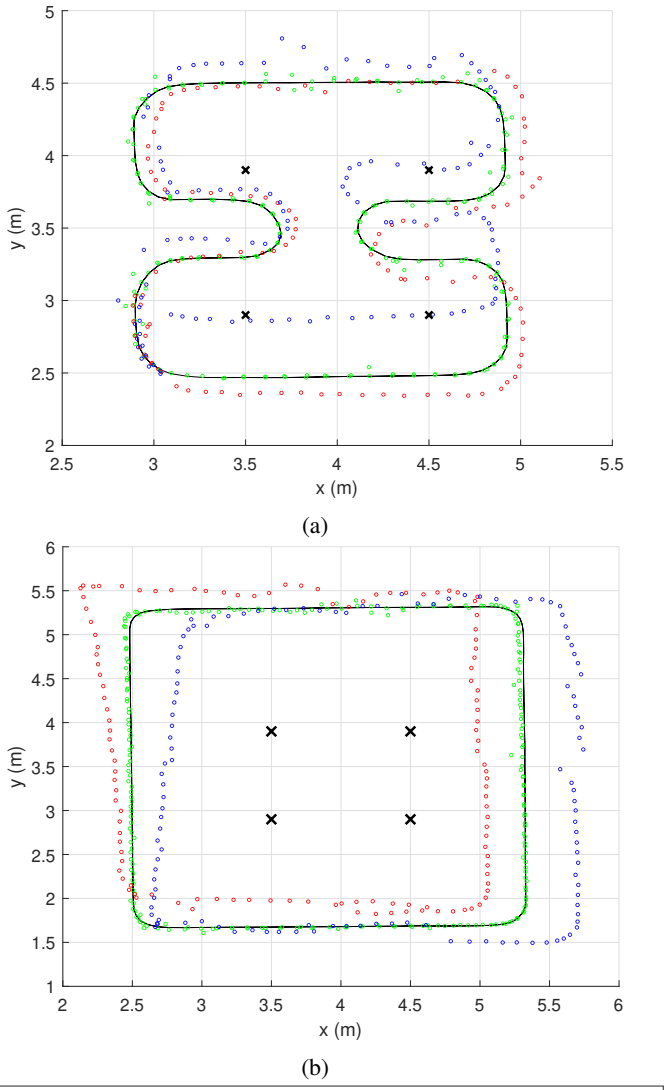

Fig. 6: Estimated positions with the IR and US measurements, as well as the merged solution from the EKF when introducing outliers for the: a) inner trajectory; b) outer trajectory.

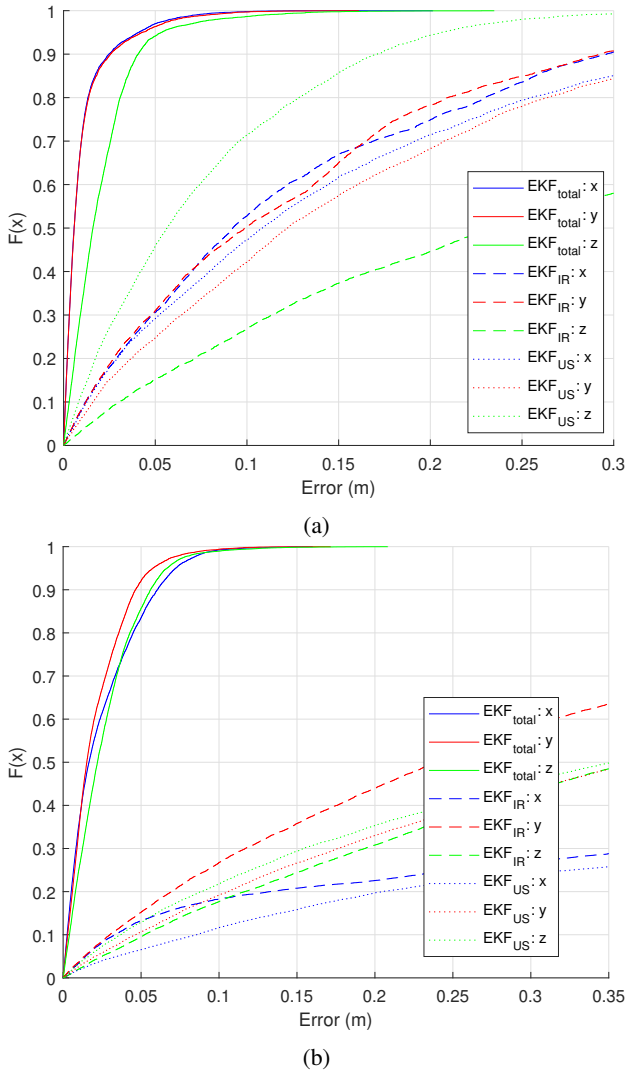

Fig. 7: CDF of the absolute positioning errors for: a) the inner trajectory; and b) the outer trajectory in Fig. 6.

the systems (IR or US). The merged solution from the EKF obtains absolute positioning errors below 4 cm and 6 cm, in 90 % of cases, for the inner and outer trajectory, respectively.

Another analysis is presented in Figs. 8 and 9. The two aforementioned trajectories are now analysed again, with the difference that we now simulate a data acquisition failure, where two IR LEDs or two US beacons are not used in 25 % of the measured points each (for the IR and the US systems, respectively). As in the previous analysis, since the not-used transmitters are randomly selected, both IR and US transmitters can be not considered at certain points at the same time. Fig. 8 presents the EKF estimated positions in the XY plane for both trajectories using either the IR or US system (red or blue dots, respectively), or both of them (green dots).

In addition, Fig. 9 presents the CDF of the obtained errors for both trajectories, achieving absolute positioning errors in all coordinates below 1 cm in 90 % of cases for both trajectories when combining IR and US measurements in the EKF. Furthermore, note that an analytic algorithm such as trilateration does not provide a position unless it has at least three LEDs or beacons available. Therefore, by using the EKF we are positioning with the combined system without having the minimum requirements for trilateration, thus enhancing the feasibility and availability of the proposal.

V. Experimental Results

The experimental tests have been carried out in a room of $8 \times 7 \times 3.4$ m^3, under normal light and acoustic noise conditions. The IR beacons ILH-IW01–85NL–SC201-WIR200 [45] have been placed in the central part of the ceiling of the room, distributed at the four corners of a square with a 1.2 m long side. Each LED has a Field-of-View (FoV) of 150º. Note that this distribution allows all LEDs to cover the unit cell of 2×2 m^2. If the LEDs are placed in a square with a shorter side, they may not cover the corners of the unit cell. On the other hand, if a much longer side is selected, it may occur that the centre of the unit cell is not covered by all LEDs. The

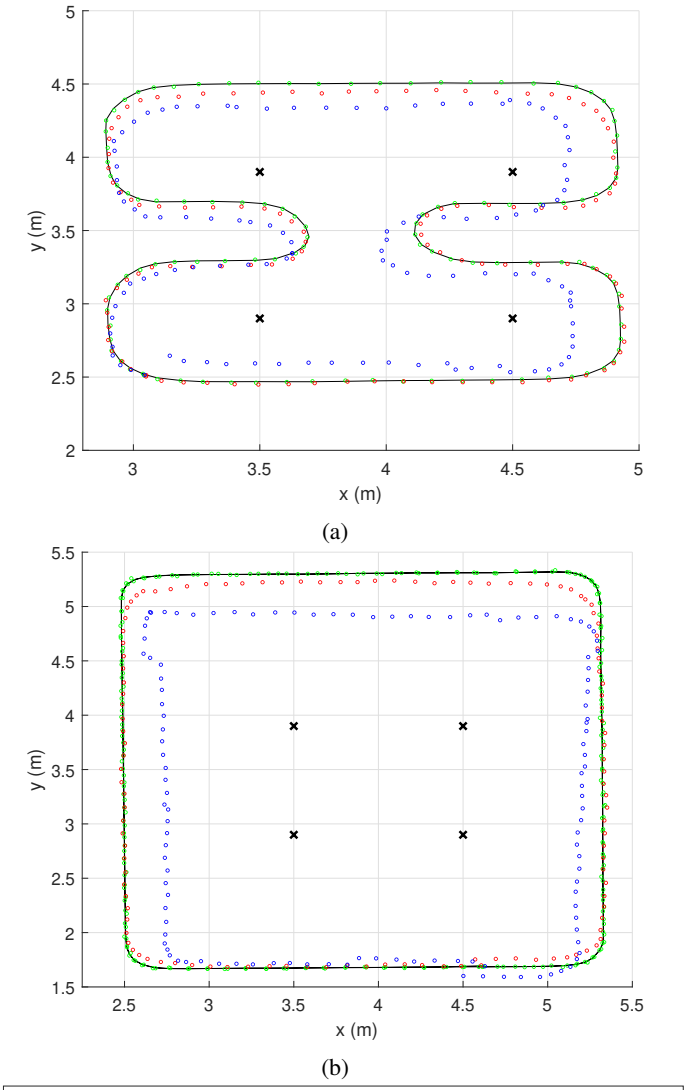

Fig. 8: Estimated positions with IR and US measurements, as well as the merged solution from the EKF when introducing a data acquisition failure for: a) the inner trajectory; and b) the outer trajectory.

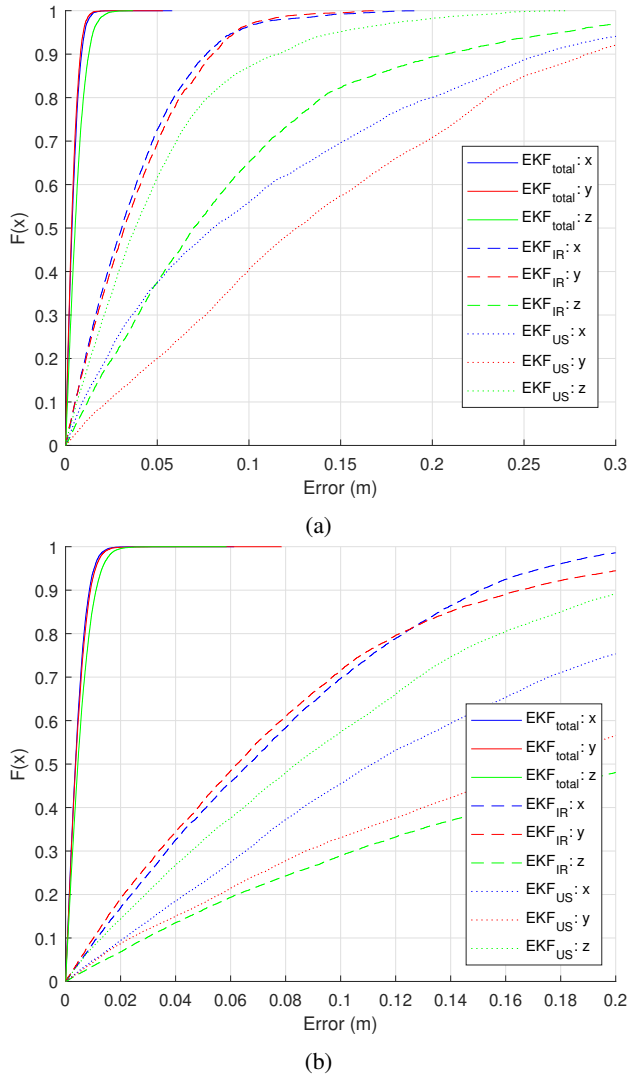

Fig. 9: CDF of the absolute positioning errors for: a) the inner trajectory; and b) outer trajectory in Fig. 8.

ultrasonic beacons Prowave (328ST160) [46] are at the corners of the room. Each beacon has a FoV of 120º.The distribution of the US beacons provide coverage to the whole room. The infrared (IR) and ultrasound (US) receivers are placed on top of a line-following robot on the room floor, as shown in Fig. 10. A high-precision system based on a Leica TS60 total station [47] and a 360º mini prism is used to determine the ground-truth of the analysed trajectories. This system obtains the 3D position of the desired object with an accuracy of 1.5 mm. Note that the acquisitions of the IR and US signals are simultaneous.

The IR receiver has been calibrated, so that all the parameters in (1) are known. These parameters are obtained by minimizing the positioning error using iterative methods, such as a Branch and Bound algorithm and a Linear Least Squares algorithm. The aperture height is set at $h_{ap} = 2.2$ mm, the focal length adjustment is $\lambda = 1.25$, the aperture misalignment is set at $\delta = 0.1$ rad, the aperture length is $l = 2.75$ mm, and the optical centre is located at $(c_x, c_y) = (0.05, 0.02)$ mm.

The inner trajectory analyzed in simulations is now analysed experimentally. Fig. 11 show the experimental measurements obtained in the XY plane using an IR or US trilateration algorithm, and the EKF that merges both IR and US system. These trilateration and triangulation algorithms have already been introduced in Section II. The ground-truth is plotted in a black line, and the projections of the IR beacons are presented with black crosses. It is noticeable that those sections in the trajectory where the performance of the positioning systems degrades accumulate a large number of outliers. This is due to some issues in the signals' transmission (multipath conditions, low SNR, reflections, etc.). Particularly, there are more outliers in the US system than in the IR system throughout the test area. It should be remarked that, although the coverage conditions are similar, the ultrasound beacons are further away as they were installed at the corners of the room. On the other hand, the IR system has a particular area in the upper

Fig. 10: Experimental validation scenario for the proposed positioning systems.

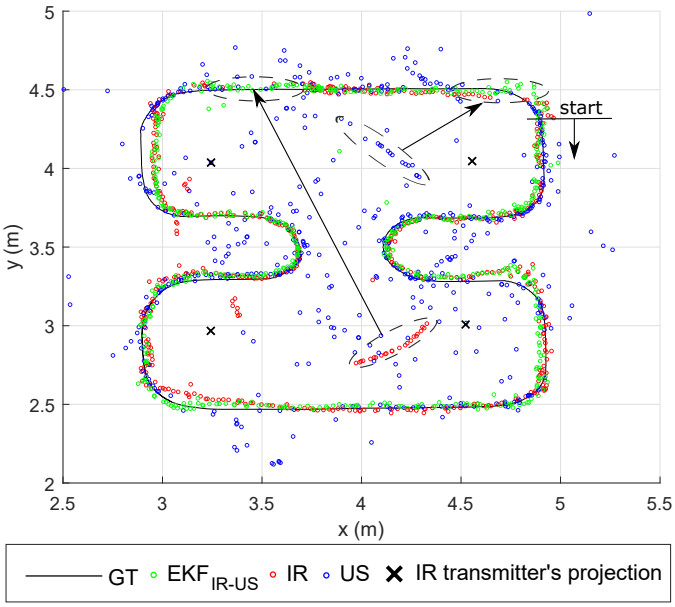

Fig. 11: Experimental estimated positions with the IR and US systems, as well as with the merged solution based on the EKF for the inner trajectory.

left corner that does not have any coverage, marked with a doted black line in Fig. 11. Combining the results from both systems with the EKF, the IR-US system improves positioning availability along the whole path. It is worth noting that the odometry from the mobile robot has not been included yet, despite the fact that it might also help filter or mitigate the dispersion of values along the trajectory.

As detailed in Section III-A, the first step in the proposed positioning algorithm is to initialize the EKF. The measurement noise matrices for the IR system $\mathbf{R}_{IR}$ and the US one $\mathbf{R}_{US}$ are a diagonal matrix with all values $\sigma^2_{x_r} = \sigma^2_{y_r} = 10^{-4}$ mm^2, $\sigma_{x_r y_r} = 0$ mm^2 and $\sigma^2_d = 10^{-6}$ m^2, respectively; the process noise covariance matrix $\mathbf{Q}$ is a diagonal matrix with all values equal to $\sigma^2_x = \sigma^2_y = \sigma^2_z = \sigma^2_\gamma = 10^{-6}$ m^2; and the initial transition matrix $\mathbf{P}_0$ has been set as a diagonal with all values $\sigma^2 = 10^{-2}$. All these matrices have been adjusted experimentally.

In the example shown in Fig. 11, the percentage of outliers, for only IR, only US, and both systems simultaneously, are 2.22 %, 24.74 % and 1.86 %, respectively. Note that since the IR-US EKF combined system has an availability of 100%, the proposed system increases the availability of the IR and US system in a 4.08% and a 26.6%, respectively. Among the IR outliers, 0.74 %, 0 %, 0.74 % and 0 % of acquisitions presents a lack of LEDs 1, 2, 3 and 4, respectively. Additionally, 0.74 % of the acquisitions present two or more simultaneous IR LEDs failures. The average error of the image points for the outliers is 1.39 mm. On the other hand, regarding the US outliers, 4.18 %, 2.91 %, 5.82 % and 4.91 % of acquisitions are related to a failure of beacons 1, 2, 3 and 4. Additionally, 6.92 % of the acquisitions present two or more simultaneous US beacon failures. The average error of the measured distance for the outliers is 1.66 m. A summary of the percentage of outliers per beacon and positioning system is presented in Table I.

TABLE I: Summary of the obtained outliers for all the beacons and systems.

System	Beacon	Percentage of outliers	Average absolute error*
IR	1	0.74	1.39 mm
	2	0	
	3	0.74	
	4	0	
	Several beacons	0.74	
US	1	4.18	1.66 m
	2	2.91	
	3	5.82	
	4	4.91	
	Several beacons	6.92	

*IR average absolute error of image points (x_r, y_r) and US average absolute error in the distance d between the US emitter and receiver.

Fig. 12 shows the Cumulative Distribution Functions (CDFs) of the absolute errors for each coordinate (x, y, z) for the position estimation, considering both positioning systems independently, as well as the combined IR-US solution. The absolute error has been determined as the distance between each estimated point and the nearest timestamped ground-truth point. It can be observed that the absolute positioning errors in 90 % of the IR estimated positions for coordinates x, y, z are 0.04 m, 0.06 m and 0.58 m, respectively; 0.08 m, 0.28 m and 0.80 m for coordinates x, y, z in the US estimated positions; and 0.04 m, 0.04 m and 0.44 m for coordinates x, y, z in the IR-US EKF estimated positions. More information is detailed in Table II.

The obtained results for the tightly-coupled EKF can also be compared with the obtained results for the loosly-coupled

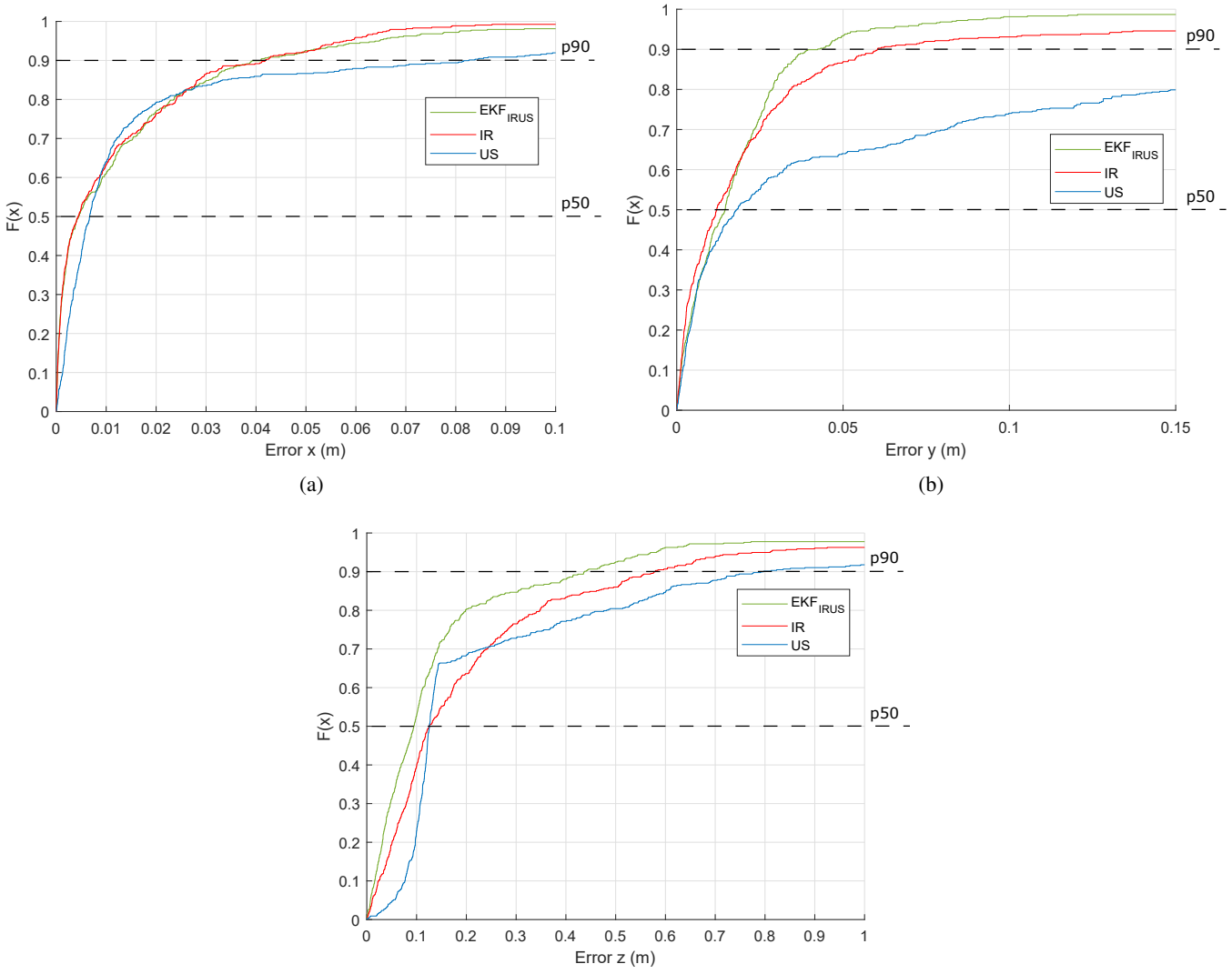

Fig. 12: CDF of the experimental absolute positioning errors, obtained by using a trilateration algorithm for the IR and US measurements and the proposed EKF for the merged approach, in coordinates: a) x; b) y; and c) z.

TABLE II: Summary of the obtained absolute positioning errors for all the coordinates and positioning systems.

LPS	Coordinates	Absolute Error (m)	
		p50	p90
IR	x	0.004	0.041
	y	0.012	0.061
	z	0.126	0.579
US	x	0.007	0.082
	y	0.017	0.277
	z	0.126	0.796
IR-US EKF	x	0.004	0.041
	y	0.014	0.042
	z	0.094	0.437

EKF. In particular, the loosly-coupled EKF was analysed in [35], achieving absolute errors below 7 cm in 90% of cases. The achieved results from both methods are detailed in Fig. 13.

Finally, Fig. 14 details the rotational angle γ obtained using the IR-US EKF algorithm. Note that only the IR system provides the value of γ. Nevertheless, this angle is included in the vector state of the EKF and then provided at each iteration.

It is worth mentioning that the algorithm takes 162.4 ms on average to run on a MATLAB environment with an Intel Core i7-8750H PC. With a measurement frequency of 5Hz (period of 200ms), there is enough time to estimate the mobile robot's position. Future work will focus on improving the efficiency of the algorithm.

VI. Conclusions

This work has presented the evaluation and implementation for the merging of an infrared (IR) and an ultrasonic (US) local positioning systems (LPS). The infrared-based LPS has been described, consisting of a set of LED-based beacons and a mobile QADA receiver, whereas the ultrasound-based LPS is based on a set of US beacons and a mobile MEMS receiver. Both systems are synchronised to start each measurement at the same time. The particularization of a tightly

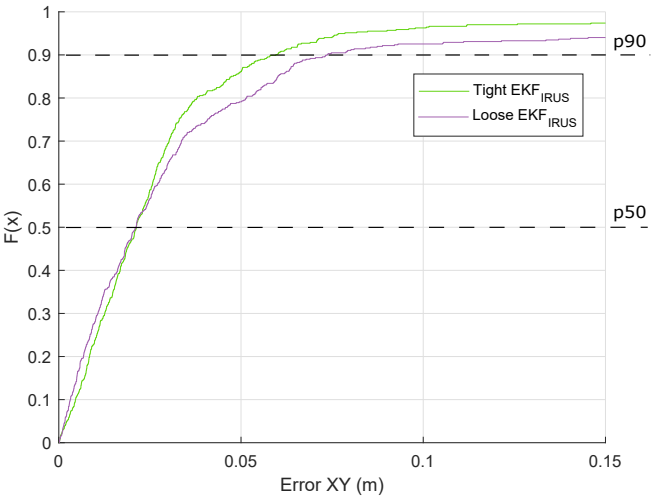

Fig. 13: CDF of the experimental absolute positioning errors, obtained by using a loosely-coupled EKF [35] and the proposed tightly-coupled IR-US EKF in plane XY.

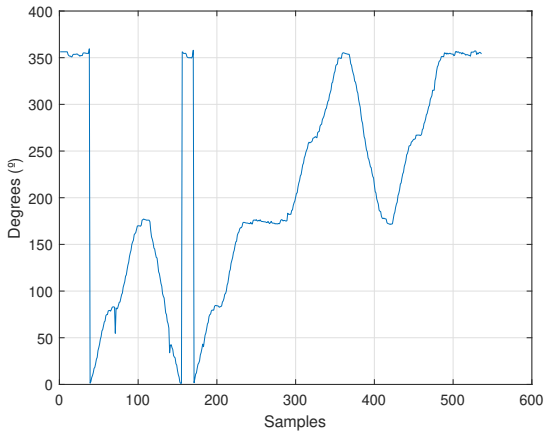

Fig. 14: Experimental estimated rotational angle γ obtained by the merged solution based on the EKF (since this angle is also included in the state vector).

coupled Extended Kalman filter (EKF) has been proposed in order to merge the measurements from both LPSs into a more robust, reliable and feasible position estimation of the receiver. The system has been tested in simulations, with a high percentage of outliers or lost measurements, in an area of 4×4 m^2, where the EKF achieves absolute positioning errors in 90% of cases below 4 cm for the inner trajectory even when introducing outliers or data acquisition failures on any of the IR/US systems. The experimental tests have been carried out in a large room (8×7 m^2) with a height of 3.4 m, with a central test area. The IRLPS solution has a higher restriction in the provided coverage, resulting in an earlier reduction of the performance while moving towards the room's corners. On the other hand, the accuracy of the IRLPS is higher than the ULPS solution in the central area, likely due to the fact that the ultrasonic beacons are installed farther away from that central area. Experimental results reveal that the position errors achieved when merging both positioning systems with an EKF are less than 4 cm in 90% of cases for coordinates x and y, improving the IR and US systems when they work independently. In addition, the IR and US systems are unable to position the mobile robot in 4.08% and 26.60% of locations, whereas the combined IR-US system has a 100% of availability.

REFERENCES

[1] R. Mautz, *Indoor positioning technologies*. PhD thesis, ETH Zurich, Zurich, 2012.

[2] J. Torres-Sospedra, R. Montoliu, S. Trilles Oliver, O. Belmonte Fernández, and J. Huerta, "Comprehensive Analysis of Distance and Similarity Measures for Wi-Fi Fingerprinting Indoor Positioning Systems," *Expert Systems with Applications*, vol. 42, pp. 9263–9278, 12 2015.

[3] F. Aranda-Polo, J. Parades, T. A. Benítez, and F. Á. Franco, "Improving BLE deterministic fingerprinting by using a weighted k-NN algorithm over filtered RSSI data," in *Proc. International Conference on Indoor Positioning and Indoor Navigation (IPIN 2019)*, pp. 431–438, 2019.

[4] T.-M. T. Dinh, N.-S. Duong, and Q.-T. Nguyen, "Developing a novel real-time indoor positioning system based on ble beacons and smartphone sensors," *IEEE Sensors Journal*, vol. 21, no. 20, pp. 23055–23068, 2021.

[5] C. Wang, A. Xu, J. Kuang, X. Sui, Y. Hao, and X. Niu, "A high-accuracy indoor localization system and applications based on tightly coupled uwb/ins/floor map integration," *IEEE Sensors Journal*, vol. 21, no. 16, pp. 18166–18177, 2021.

[6] D. Gualda, J. M. Villadangos, J. Ureña, A. R. J. Ruiz, F. Seco, and Á. Hernández, "Indoor positioning in large environments: ultrasonic and UWB technologies," in *Proc. International Conference on Indoor Positioning and Indoor Navigation (IPIN 2019)*, pp. 1–8, 2019.

[7] C. Wang, L. Wang, X. Chi, S. Liu, W. Shi, and J. Deng, "The research of indoor positioning based on visible light communication," *China Communications*, vol. 12, no. 8, pp. 85–92, 2015.

[8] T. Q. Wang, Y. A. Sekercioglu, A. Neild, and J. Armstrong, "Position Accuracy of Time-of-Arrival Based Ranging Using Visible Light With Application in Indoor Localization Systems," *Journal of Lightwave Technology*, vol. 31, no. 20, pp. 3302–3308, 2013.

[9] M. Maheepala, A. Z. Kouzani, and M. A. Joordens, "Light-based indoor positioning systems: A review," *IEEE Sensors Journal*, vol. 20, no. 8, pp. 3971–3995, 2020.

[10] F. Alam, M. T. Chew, T. Wenge, and G. S. Gupta, "An Accurate Visible Light Positioning System Using Regenerated Fingerprint Database Based on Calibrated Propagation Model," *IEEE Transactions on Instrumentation and Measurement*, vol. 68, no. 8, pp. 2714–2723, 2019.

[11] P. H. Pathak, X. Feng, P. Hu, and P. Mohapatra, "Visible Light Communication, Networking, and Sensing: A Survey, Potential and Challenges," *IEEE Communications Surveys and Tutorials*, vol. 17, no. 4, pp. 2047–2077, 2015.

[12] N. Knudde, W. Raes, J. De Bruycker, T. Dhaene, and N. Stevens, "Data-Efficient Gaussian Process Regression for Accurate Visible Light Positioning," *IEEE Communications Letters*, vol. 24, no. 8, pp. 1705–1709, 2020.

[13] S. Bastiaens, W. Raes, N. Stevens, L. Martens, W. Joseph, and D. Plets, "Impact of a Photodiode's Angular Characteristics on RSS-Based VLP Accuracy," *IEEE Access*, vol. 8, pp. 83116–83130, 2020.

[14] S. Cincotta, C. He, A. Neild, and J. Armstrong, "Indoor visible light positioning: Overcoming the practical limitations of the quadrant angular diversity aperture receiver (QADA) by using the two-stage QADA-plus receiver," *Sensors (Switzerland)*, vol. 19, no. 4, 2019.

[15] E. Aparicio-Esteve, Á. Hernández, and J. Ureña, "Design, Calibration, and Evaluation of a Long-Range 3-D Infrared Positioning System Based on Encoding Techniques," *IEEE Transactions on Instrumentation and Measurement*, vol. vol. 70, pp. 1–13, 2021.

[16] E. Bernardes, S. Viollet, and T. Raharijaona, "A Three-Photo-Detector Optical Sensor Accurately Localizes a Mobile Robot Indoors by Using Two Infrared Light-Emitting Diodes," *IEEE Access*, vol. 8, pp. 87490–87503, 2020.

[17] S. Cincotta, C. He, A. Neild, and J. Armstrong, "QADA-PLUS: A Novel Two-Stage Receiver for Visible Light Positioning," *IPIN 2018 - 9th International Conference on Indoor Positioning and Indoor Navigation*, no. September, pp. 24–27, 2018.

[18] Á. De-La-Llana-Calvo, J.-L. Lázaro-Galilea, A. Gardel-Vicente, D. Salido-Monzú, I. Bravo-Muñoz, A. Iamnitchi, and R. Gil-Vera, "Weak Calibration of a Visible Light Positioning System Based on a Position-Sensitive Detector: Positioning Error Assessment," *Sensors*, vol. 21, no. 11, 2021.

[19] T. Q. Wang, R. J. Green, and J. Armstrong, "Prism array-based receiver with application in MIMO indoor optical wireless communications," in *2014 16th International Conference on Transparent Optical Networks (ICTON)*, pp. 1–4, 2014.

[20] B. Zhu, Z. Zhu, Y. Wang, and J. Cheng, "Optimal Optical Omnidirectional Angle-of-Arrival Estimator With Complementary Photodiodes," *Journal of Lightwave Technology*, vol. 37, no. 13, pp. 2932–2945, 2019.

[21] H. Steendam, T. Q. Wang, and J. Armstrong, "Theoretical lower bound for indoor visible light positioning using received signal strength measurements and an aperture-based receiver," *Journal of Lightwave Technology*, vol. 35, no. 2, pp. 309–319, 2017.

[22] A. Ward, A. Jones, and A. Hopper, "A new location technique for the active office," *IEEE Personal Communications*, vol. 4, no. 5, pp. 42–47, 1997.

[23] N. B. Priyantha, A. Chakraborty, and H. Balakrishnan, "The Cricket Location-Support System," in *Proc. of the 6th Ann. Int. Conf. on Mobile Computing and Networking*, MobiCom '00, (New York, NY, USA), p. 32–43, Association for Computing Machinery, 2000.

[24] I. Toru, Y. Yasuda, S. Sato, S. Izumi, and H. Kawaguchi, "Millimeter-precision ultrasonic dsss positioning technique with geometric triangle constraint," *IEEE Sensors Journal*, vol. 22, no. 16, pp. 16202–16211, 2022.

[25] M.-H. Kang and B.-G. Lim, "Development of a practical foolproof system using ultrasonic local positioning," *Measurement*, vol. 79, pp. 1–14, 2016.

[26] F. Gholami, E. Khanmirza, and M. Riahi, "Real-time obstacle detection by stereo vision and ultrasonic data fusion," *Measurement*, vol. 190, p. 110718, 2022.

[27] Á. Hernández, E. García, D. Gualda, J. M. Villadangos, F. Nombela, and J. Ureña, "FPGA-Based Architecture for Managing Ultrasonic Beacons in a Local Positioning System," *IEEE Transactions on Instrumentation and Measurement*, vol. 66, no. 8, pp. 1954–1964, 2017.

[28] J. Ureña, Á. Hernández, J. J. García, J. M. Villadangos, M. Carmen Pérez, D. Gualda, F. J. Álvarez, and T. Aguilera, "Acoustic Local Positioning With Encoded Emission Beacons," *Proceedings of the IEEE*, vol. 106, no. 6, pp. 1042–1062, 2018.

[29] M. Deffenbaugh, J. Bellingham, and H. Schmidt, "The relationship between spherical and hyperbolic positioning," in *OCEANS 96 MTS/IEEE Conference Proceedings. The Coastal Ocean - Prospects for the 21st Century*, vol. 2, pp. 590–595 vol.2, 1996.

[30] D. Gualda, J. Ureña, J. C. García, E. García, and J. Alcalá, "Simultaneous calibration and navigation (SCAN) of multiple ultrasonic local positioning systems," *Information Fusion*, vol. 45, pp. 53–65, 2019.

[31] E. Bernardes, S. Viollet, and T. Raharijaona, "A Three-Photo-Detector Optical Sensor Accurately Localizes a Mobile Robot Indoors by Using Two Infrared Light-Emitting Diodes," *IEEE Access*, vol. 8, pp. 87490–87503, 2020.

[32] X. Chen, Y. Xu, Q. Li, J. Tang, and C. Shen, "Improving ultrasonic-based seamless navigation for indoor mobile robots utilizing EKF and LS-SVM," *Measurement*, vol. 92, pp. 243–251, 2016.

[33] D. Esslinger, M. Oberdorfer, L. Kleckner, O. Sawodny, and C. Tarín, "Receiver Self-Localization for an Opto-Acoustic and Inertial Indoor Localization System," in *2020 IEEE/ASME International Conference on Advanced Intelligent Mechatronics (AIM)*, pp. 540–546, 2020.

[34] G. Falco, M. Pini, and G. Marucco, "Loose and tight gnss/ins integrations: Comparison of performance assessed in real urban scenarios," *Sensors*, vol. 17, no. 2, 2017.

[35] E. Aparicio-Esteve, J. M. Villadangos, Á. Hernández, and J. Ureña, "Experimental Evaluation of an IR and US Multi-Sensory Positioning Fusion Method," in *WiP Proc. International Conference on Indoor Positioning and Indoor Navigation (IPIN 2021), CEUR Workshop Proceedings (CEUR-WS.org)*, pp. 1–13, 2021.

[36] D.-C. Lin, C.-W. Chow, C.-W. Peng, T.-Y. Hung, Y.-H. Chang, S.-H. Song, Y.-S. Lin, Y. Liu, and K.-H. Lin, "Positioning Unit Cell Model Duplication With Residual Concatenation Neural Network (RCNN) and Transfer Learning for Visible Light Positioning (VLP)," *Journal of Lightwave Technology*, vol. 39, no. 20, pp. 6366–6372, 2021.

[37] D. Gualda, J. Ureña, and E. García, "Partially Constrained Extended Kalman Filter for Navigation Including Mapping Information," *IEEE Sensors Journal*, vol. 16, no. 24, pp. 9036–9046, 2016.

[38] E. Aparicio-Esteve, A. Hernández, J. Ureña, and J. M. Villadangos, "Visible Light Positioning System Based on a Quadrant Photodiode and Encoding Techniques," *IEEE Transactions on Instrumentation and Measurement*, vol. 69, no. 8, pp. 5589–5603, 2020.

[39] F. S. Inc., "Series 6 Data Sheet Quad Sum and Difference Amplifier, Part Description QP50-6-18u-SD2, Product Specification," 2012.

[40] STMicroelectronics, "STM32F469IDiscovery," *Product Specification*, pp. 1–40, 2015.

[41] E. Aparicio-Esteve, Á. Hernández, and J. Ureña, "Design, Calibration, and Evaluation of a Long-Range 3-D Infrared Positioning System Based on Encoding Techniques," *IEEE Transactions on Instrumentation and Measurement*, vol. vol. 70, pp. 1–13, 2021.

[42] E. Aparicio-Esteve, Á. Hernández, J. Ureña, J. M. Villadangos, and F. Ciudad, "Estimation of the Polar Angle in a 3D Infrared Indoor Positioning System based on a QADA receiver," *Proc. of 2019 International Conference on Indoor Positioning and Indoor Navigation (IPIN 2019)*, pp. 1–8, 2019.

[43] L. Knowles Acoustics, "Amplified "Ultra-Mini" SiSonicTM Microphone SpecificationWith MaxRF Protection," *Product Specification*, 2012.

[44] E. Aparicio-Esteve, D. Moltó, J. Ureña, Á. Hernández, and F. Espinosa, "Dynamic Adjustment of Measurement Noise Covariance Matrix in an Infrared-based Positioning and Tracking System," in *Proc. International Conference on Indoor Positioning and Indoor Navigation (IPIN 2022)*, pp. 1–8, 2022.

[45] Oslon, "OSLON® 1 PowerStar IR, IGS Version," *Product Specification*, pp. 1–7, 2015.

[46] J. M. Villladangos, J. Ureña, J. J. García, M. Mazo, Hernández, A. Jiménez, D. Ruíz, and C. D. Marziani, "Measuring time-of-flight in an ultrasonic lps system using generalized cross-correlation," *Sensors*, vol. 11, no. 11, pp. 10326–10342, 2011.

[47] L. Geosystems, "Leica nova ts60," *Product Specification*, 2014.